16th International Symposium on Particle Image Velocimetry – ISPIV 2025
June 26–28, 2025, Tokyo, Japan

Event-based imaging velocimetry for jet flow control

L. Franceschelli[1*], E. Amico[2], M. Raiola[1], C.E. Willert[3], J. Serpieri[2], G. Cafiero[2], S. Discetti[1]

[1] Department of Aerospace Engineering, Universidad Carlos III de Madrid, Avda. Universidad 30, Leganès, 28911, Spain

[2] Department of Mechanical and Aerospace Engineering, Politecnico di Torino, Corso Duca degli Abruzzi 24, Turin, 10129, Italy

[3] DLR Institute of Propulsion Technology, German Aerospace Center, Linder Höhe, Köln, 51170, Germany

[*] lfrances@ing.uc3m.es

Abstract

This study presents the use of Event-Based Imaging Velocimetry (EBIV) for experimental jet flow control, integrating a Bayesian optimization strategy to enhance mixing in a turbulent round jet. Velocity fields are acquired using a pulsed low-power laser and an event-based vision camera, enabling time-resolved, full-field measurements at kilohertz rates. A cost function based on the spatial average of the turbulent kinetic energy is computed from EBIV measurements and used to optimize the actuation parameters of two synthetic jets located inside the nozzle, in the plane of the EBIV measurement. The proposed approach allows optimizing the control in a non-intrusive manner, with minimal sensor cost and data latency. The impact of the optimal actuation is further assessed using Spectral Proper Orthogonal Decomposition, which reveals the excitation of coherent structures across a broad spectral range, including harmonics not directly excited. These results demonstrate the potential of EBIV as a compact, high-throughput sensor tool for data-driven flow control and the development of active control strategies.

1 Introduction

Jet flows are fundamental in numerous industrial applications, influencing propulsion efficiency, mixing performance, and thermal regulation in aerospace, combustion, and chemical processes. Effective control of these flows can reduce noise, improve fuel-air mixing, and enhance overall system performance. To this end, Active Flow Control (AFC) strategies, supported by data-driven methods, are being developed to reduce energy losses and enhance adaptability in complex and unsteady flow environments.

Traditionally, jet flow control optimization has relied on high-frequency, single-point sensing methods such as hot-wire anemometry and pressure transducers (Parekh et al., 1996; Zhou et al., 2020). These techniques provide high-bandwidth data—often at kilohertz rates—making them suitable for feedback control (Audiffred et al., 2024; Shaqarin et al., 2024). However, their intrusive nature and limitation to point-wise measurements can hinder the capture of global flow dynamics. In jet flows, coherent structures such as vortex rings and shear-layer instabilities play a dominant role in determining mixing, noise radiation, and flow development. Capturing these structures is essential for effective control.

Non-intrusive optical methods like Particle Image Velocimetry (PIV) have been used to obtain full-field measurements of velocity and vorticity, offering rich spatial information that enhances state estimation and control performance (Brunton and Noack, 2015). Yet, the high data rates, significant post-processing requirements, and cost of high-speed cameras make PIV challenging to integrate into control loops. Even applications as sensor for optimization of open-loop controllers is often prohibitive due to the high cost of assessing each single control law.

Event-Based Imaging Velocimetry (EBIV), based on Event-Based Vision (EBV) sensors, offers a promising solution to embed PIV in flow control. EBV sensors asynchronously detect changes in brightness at each pixel, allowing for high temporal resolution with low data rates and reduced latency (Gallego et al., 2022). Pulsed-EBIV (Willert, 2023) further improves the method by synchronizing event acquisition with pulsed illumination, addressing limitations related to sensor latency and noise. Recent studies comparing EBIV and PIV measurements in air flows (Franceschelli et al., 2024) demonstrated the capability of EBIV to accurately capture key flow features and low-order flow representations, confirming its potential as a fast and low-cost alternative for flow sensing.

The present study explores the use of EBIV as a flow diagnostic and evaluation tool within an open-loop flow control experiment. The goal is to optimize actuation parameters to enhance mixing in a turbulent round jet. A Bayesian Optimization (BO) algorithm (Blanchard et al., 2021; Mallor et al., 2024) is employed to iteratively identify optimal control settings based on a reward function derived from EBIV velocity fields, namely the maximization of the Turbulent Kinetic Energy (TKE).

The experimental setup consists of an air jet facility equipped with six synthetic jet actuators distributed azimuthally around the nozzle exit, and two loudspeakers in the stagnation chambers, providing acoustic forcing. However, for this study, the control input is limited to two actuators located in the plane of EBIV measurements. This reduced test case enables symmetric actuation relative to the measurement plane and allows for efficient exploration of the parameter space, consisting of the two actuation frequencies and one relative phase delay.

EBIV measurements are performed using a low-power pulsed laser module and an event-based camera operating at kilohertz effective rates. The reward function is defined based on the spatial average of TKE within a selected region of the flow field, capturing key topological features relevant to mixing enhancement. This approach provides a rich and informative control signal without requiring intrusive probes or extensive post-processing.

Overall, the integration of EBIV with BO offers a scalable, efficient framework for experimental flow control, bridging the gap between high-resolution sensing and data-driven control design.

2 Experimental Set-up

2.1 Jet facility

The experiments are conducted in the air jet facility located inside the anechoic chamber at *Universidad Carlos III de Madrid* (Moreno et al., 2024). The setup consists of a round jet issuing from a nozzle with an exit diameter of $D = 20\,\mathrm{mm}$. To ensure turbulent boundary layer conditions in the nozzle, a tripping device is installed at the beginning of the nozzle contraction section. The flow is seeded with $1\,\mu\mathrm{m}$ diameter droplets of Di-Ethyl-Hexyl-Sebacate (DEHS). The total mass flow is generated by combining two pressurized lines: one supplying clean air and the other seeded air. Both lines are regulated using dedicated mass-flow controllers, which maintain a constant total mass flow rate and consistent seeding density throughout the experimental campaign.

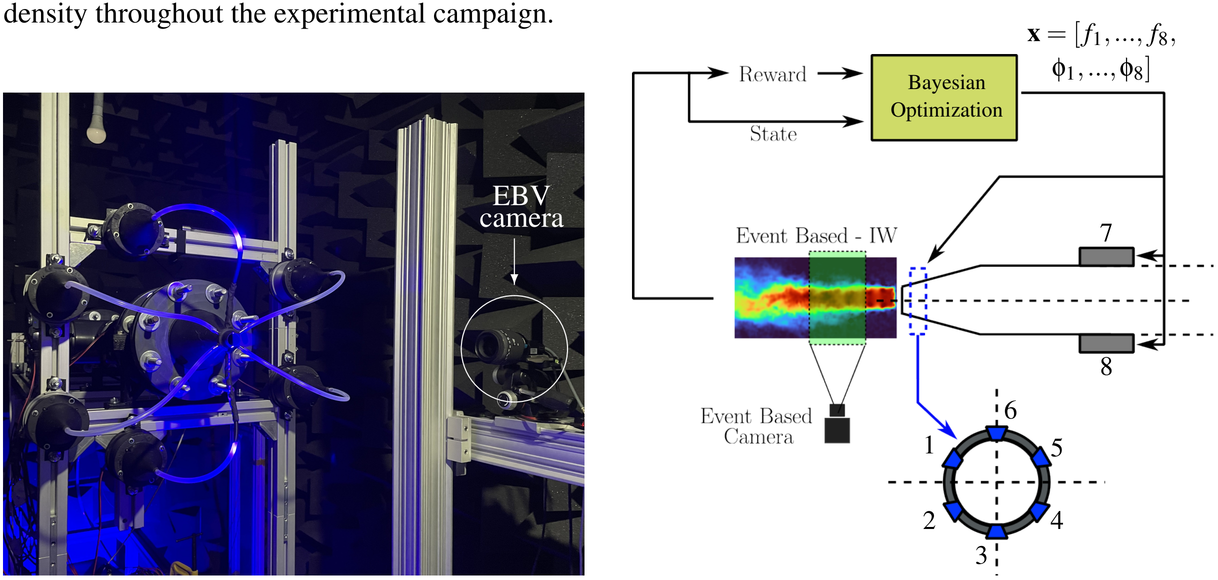

Figure 1: Experimental set-up (left) showing the jet facility and event-based camera, and corresponding EBIV-based control architecture (right) implemented for jet flow control experiments.

A low-cost laser module (Lasertree LT-4LDS-V2), originally developed for engraving applications and delivering an optical power of 20 W, is used for flow illumination. The laser beam is pulsed and shaped into a thin light sheet of approximately 1 mm thickness through a set of lenses. The resulting laser plane is aligned with the longitudinal midplane of the jet.

Flow measurements are acquired using a Prophesee EVK-4 EBV camera featuring the IMX636 sensor, with a full resolution of 1280×720 pixels[2]. The sensor sensitivity can be tuned to specific experimental conditions by adjusting its internal biases. To maximize the usable bandwidth for positive events only—which are the only events useful for EBIV applications—the biases are typically configured to suppress negative events entirely. In this setup, the biases were set as follows: Diff-ON = -56, Diff-OFF = 107, High-pass filter = 76, Low-pass filter = 31, and Refractory period = -20.

A 50 mm objective lens was used, providing a spatial resolution of approximately 19.3 pixels/mm and resulting in a field of view of approximately $3.3 \times 1.8\,\mathrm{D}^2$. The objective aperture $f_\#$ is set to 4.6. The laser module is controlled by an Analog Discovery device, which provides a square-wave signal controlling the pulsation frequency and the pulse width of the laser pulse. This signal is also sent to the EBV camera, enabling synchronization of the laser pulse with the event stream. A dedicated workstation manages the entire setup: it acquires and processes data from the EBV camera, defines the control law and its optimization, and handles the actuation.

2.2 Synthetic jet actuation

The actuation system combines two types of forcing mechanisms. First, two counter-facing loudspeakers are flush-mounted inside the stagnation chamber to provide purely acoustic excitation. Second, six synthetic jets are azimuthally distributed around the nozzle, positioned one nozzle diameter upstream of the exit. Each synthetic jet actuator consists of a loudspeaker connected to a 3D-printed waveguide. These actuators are connected to the nozzle outlet via flexible silicone tubes and can be operated independently to allow phase- and frequency-specific control.

The experimental rig is illustrated in Figure 1, highlighting the arrangement of the jet facility, actuated nozzle assembly and the EBV camera. Control signals are generated using a National Instruments Compact-RIO 9045 (cRIO) system equipped with a NI-9263 module. The signals are then amplified by an 8 indipendent channel amplifier (Sirus I-Amp 8.150). All loudspeakers used in the setup, both for the stagnation chamber and the synthetic jets, are Dayton Audio ND65-4 compact models.

A detailed characterization of the synthetic jet actuators has been performed using hot-wire anemometry, measuring the exit velocity of the jets. A mapping of the peak exit velocity U_p as a function of actuation frequency f and signal amplitude to the amplifier V_{0p} was obtained. An example of the characterization result is shown in Figure 2, showing the isolines for different desired U_p. For the current experiment, a constant U_p is imposed for all actuators. From a practical standpoint, the signal amplitude required for each loudspeaker is selected from the isoline corresponding to the target U_p, based on the chosen actuation frequency.

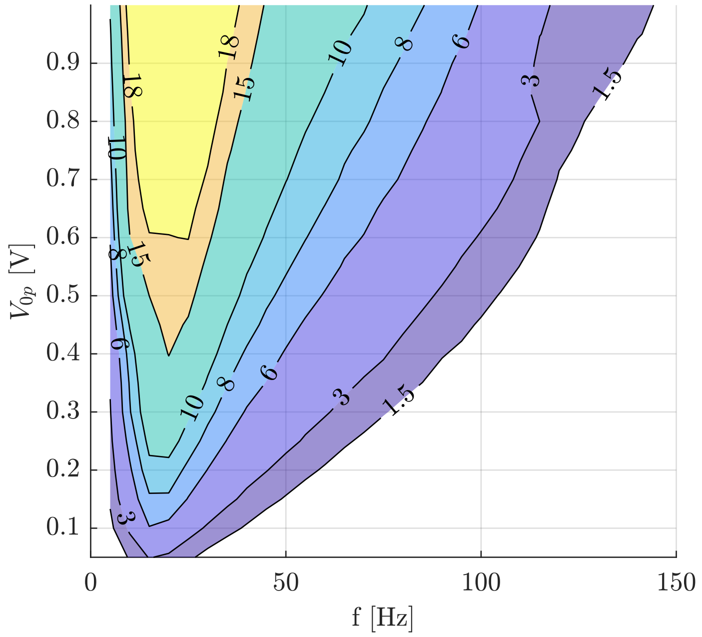

Figure 2: Characterization of the synthetic jet actuators. Isolines of the peak velocity U_p for values $U_p = \{1.5,\ 3,\ 6,\ 8,\ 10,\ 15,\ 18\}\,\mathrm{m/s}$, plotted as a function of actuation frequency f and input signal amplitude V_{0p}.

2.3 Bayesian Optimization

BO is a sample-efficient global optimization strategy for expensive black-box functions. It relies on two key components: a probabilistic surrogate model, typically a Gaussian Process (GP), and an acquisition function to guide the search (Garnett, 2023) .

Given an objective function $f(\mathbf{x}) : S \subseteq \mathbb{R}^d \to \mathbb{R}$, where f is a scalar-valued objective function that maps the input parameters $\mathbf{x}$ to a real-valued cost, and S denotes the s-dimensional input space, BO aims to solve:

$$\mathbf{x}_{\text{opt}} = \arg\min_{\mathbf{x}\in S} f(\mathbf{x}) \tag{1}$$

The observed outputs are modeled as evaluations corrupted by noise:

$$y(\mathbf{x}) = f(\mathbf{x}) + \varepsilon, \quad \varepsilon \sim \mathcal{N}(0, \sigma_\varepsilon^2) \tag{2}$$

The surrogate GP model assumes:

$$f(\mathbf{x}) \sim \mathcal{GP}(\mu(\mathbf{x}), k(\mathbf{x}, \mathbf{x}')) \tag{3}$$

with a mean function $\mu(\mathbf{x})$ (often zero) and a covariance function $k(\mathbf{x}, \mathbf{x}')$. We employ the Radial Basis Function (RBF) kernel:

$$k(\mathbf{x}, \mathbf{x}') = \sigma_f^2 \exp\left(-\frac{\|\mathbf{x} - \mathbf{x}'\|^2}{2\lambda^2}\right) \tag{4}$$

Given n observations $\mathcal{D} = \{(\mathbf{x}_i, y_i)\}_{i=1}^n$, the posterior predictive distribution at a test point $\mathbf{x}^*$ is Gaussian with:

$$\mu(\mathbf{x}^*) = \mathbf{k}_*^\top (K + \sigma_\varepsilon^2 I)^{-1} \mathbf{y} \tag{5}$$

$$\sigma^2(\mathbf{x}^*) = k(\mathbf{x}^*, \mathbf{x}^*) - \mathbf{k}_*^\top (K + \sigma_\varepsilon^2 I)^{-1} \mathbf{k}_* \tag{6}$$

where $\mathbf{k}_*$ is the vector of covariances between $\mathbf{x}^*$ and the training inputs, and K is the kernel matrix.

To guide sampling, we employ the Expected Improvement (EI) acquisition function:

$$\text{EI}(\mathbf{x}^*) = \mathbb{E}\left[\max(f_{\text{best}} - f(\mathbf{x}^*) - \xi, 0)\right] \tag{7}$$

Under Gaussian assumptions, EI has a closed-form expression:

$$\text{EI}(\mathbf{x}^*) = (f_{\text{best}} - \mu(\mathbf{x}^*) - \xi)\Phi(Z) + \sigma(\mathbf{x}^*)\phi(Z) \tag{8}$$

$$Z = \frac{f_{\text{best}} - \mu(\mathbf{x}^*) - \xi}{\sigma(\mathbf{x}^*)} \tag{9}$$

where $\Phi(\cdot)$ and $\phi(\cdot)$ denote the CDF and PDF of the standard normal distribution, respectively, and $\xi > 0$ encourages exploration.

This approach efficiently balances exploration and exploitation, making BO well-suited for optimizing costly or noisy functions.

2.4 EBIV processing

Figure 1 presents a schematic of the EBV camera integration within the control loop. The event data associated with each laser pulse are accumulated over a defined time window, termed the *accumulation time*, starting from the laser triggers and generating pseudo-images. These are then processed using conventional PIV algorithms to extract instantaneous velocity fields (Willert, 2023). At each control episode, short sequences of events are recorded, processed, and analyzed to evaluate the control cost function and determine the next control action.

More specifically, the presented results are obtained considering a jet bulk velocity $U_b = 1.8\,\text{m/s}$, resulting in a Reynolds number $Re \sim 2400$. The laser is pulsed at a frequency $f_{EBIV} = 1500\,\text{Hz}$ with a pulse width corresponding to 20% of the laser duty cycle, i.e. $130\,\mu\text{s}$. For each control episode, time-resolved sequences with a duration of 5 seconds are acquired with the EBV camera. Subsequently, a set of 500 randomly distributed pseudo-images pairs are generated. An in-house PIV software is used to process the images using a multi-pass multi-grid approach resulting in a final Interrogation Window (IW) of 32x32 pixels^2 with a 50% overlap. The camera is mounted with its short sensor side aligned along the jet axis, thereby using the full width of the sensor in the spanwise direction to capture possible large lateral expansions of the flow. This configuration results in a resolved field of view spanning approximately $1.5 < x/D < 3.1$ in the streamwise direction and $-1.6 < y/D < 1.6$ in the cross-stream direction.

The obtained two-dimensional velocity field is denoted as $U = [u; v] \in \mathbb{R}^{N_p \times N_t}$, where u and v are the streamwise and cross-stream velocity components, respectively, and N_p and N_t are the number of grid points and time snapshots. The corresponding fluctuating fields $[u'; v']$ are obtained by subtracting the mean velocity field $\bar{U}$ from each instantaneous snapshot.

The ensemble-averaged TKE field is defined as:

$$\overline{\mathrm{TKE}}(x,y) = \frac{1}{2}\left(\overline{u'^2}(x,y) + \overline{v'^2}(x,y)\right) \tag{10}$$

The overbar indicates the ensemble-averaging operation.

To enhance mixing, the optimization reward y_i is defined as the spatial average of the TKE field over a selected region $\Omega \subset \mathbb{R}^2$, which includes only the points where $\bar{u} \geq 0.2\,\bar{u}_{\max}$, with $\bar{u}_{\max}$ being the maximum value of the mean streamwise velocity field:

$$y_i = \frac{1}{|\Omega|}\int_{\Omega} \overline{\mathrm{TKE}}(x,y)\,\mathrm{d}\Omega, \quad \text{with} \quad \Omega = \{(x,y)\,|\,\bar{u}(x,y) \geq 0.2\,\bar{u}_{\max}\} \tag{11}$$

This threshold helps excluding regions where low velocities may result in artificially elevated TKE values due to measurement artifacts. The total time required to perform, acquire, process, and evaluate each control law is approximately one minute.

To ensure reliable measurements, each episode is repeated twice. If the second evaluation of y_i differs by more than 3.5% from the first, a third measurement is performed. The final reward y_i is then computed as the average of the two closest values. If no third repetition is required, y_i is taken as the average of the first two measurements. The 3.5% repeatability threshold was determined based on a dedicated measurement repeatability study.

Although the experimental setup is designed to accommodate the optimization of eight actuators, in this study we restrict our analysis to the two synthetic jets located in the EBIV measurement plane — namely, those driven by actuation signals f_3 and f_6, as indicated in Figure 1. The optimization is limited to three control parameters, i.e. $s = 3$: the actuation frequencies f_3 and f_6 of the two synthetic jets, and their relative phase shift $\Delta\phi$. This choice allows us to explore a reduced parametric space while focusing on control actions that are symmetric with respect to the EBIV evaluation plane.

Moreover, since the reward signal is based on two-dimensional measurements centered on the jet axis, the actuation space (f_3, f_6) is assumed to be symmetric. Specifically, each control input $\mathbf{x}_i = (f_3, f_6, \Delta\phi)$ is considered equivalent to its mirrored counterpart $\mathbf{x}_j = (f_6, f_3, -\Delta\phi)$, and thus both are expected to yield the same output $y_i = y_j$. As a result, the effective search space is reduced by half, further simplifying the optimization problem.

Lastly, it should be noted that providing system observations only in the longitudinal plane inherently restricts the ability to properly evaluate control actions to those that are symmetric with respect to the laser sheet. Actuation components with a net effect in the direction normal to the measurement plane may produce flow responses that cannot be reliably captured by the two-dimensional measurements. For this reason, further optimization campaigns involving additional actuators enforce a constraint of zero net injected momentum in the direction normal to the EBIV plane, ensuring that the effects of the control inputs remain observable and quantifiable within the measurement domain.

3 Results

The optimization process was repeated multiple times using different initial samples and exploration parameters ξ. Despite minor variations, the results consistently identified the same optimal regions for reward maximization. An example of the resulting optimization map is shown in Figure 3 (left), where the reward values y_i are plotted as a function of the actuation frequencies f_3 and f_6, expressed in terms of Strouhal numbers as $St_i = f_i D/U_b$. The symmetry of the map with respect to the bisector is due to the hypothesis of actuation specularity discussed in Section 2.4. As a refence value, the $y(\mathbf{x})$ evaluated in the uncontrolled case is ~ 1.75 px^2.

Overall, the actuation frequency corresponding to $St \sim 0.35$ appears to be the most effective. This frequency matches the typical vortex shedding frequency of an uncontrolled jet (Hussain and Zaman, 1981; Gutmark and Ho, 1983), suggesting that mixing enhancement is particularly sensitive to actuation tuned to Kelvin–Helmholtz instability dynamics. The global maximum in the optimization map occurs

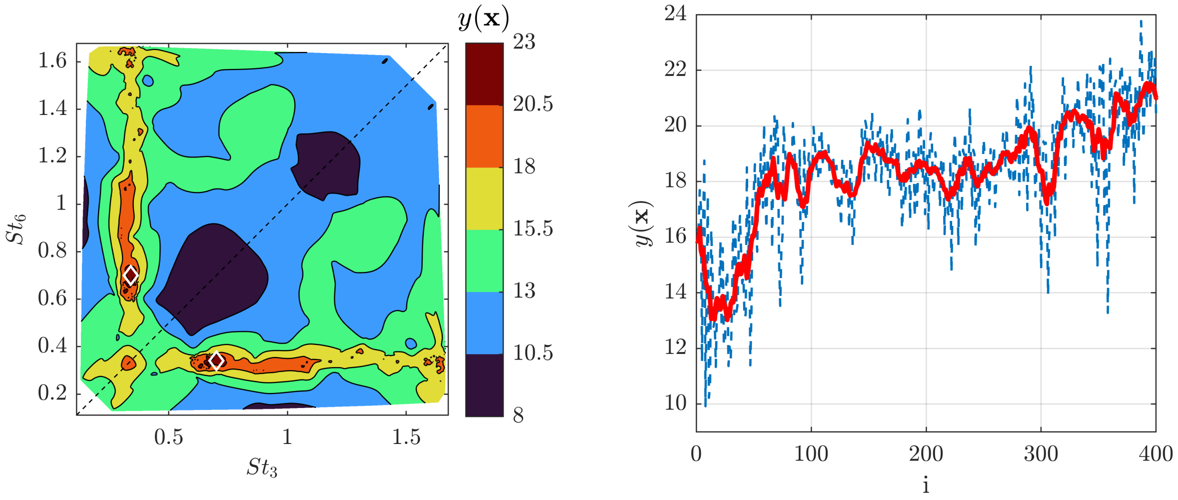

Figure 3: Left: optimization map showing the distribution of the reward $y(\mathbf{x})$ as a function of the actuation Strouhal numbers St_3 and St_6. The white diamond represent the optimal condition, compared in 3.1 to the uncontrolled case. Right: convergence history of the reward y_i over the optimization iterations, with the 10-samples moving average shown in red.

when the second actuator operates at approximately twice the frequency of the first, i.e., $St_3 \sim 0.35$ and $St_6 \sim 0.7$. The phase shift $\Delta\phi$ did not exhibit a consistent trend in relation to the reward maximization.

The right panel of Figure 3 shows the evolution of the reward y_i over the course of 400 optimization iterations. The dashed blue line represents the raw reward values, while the solid red line indicates a moving average computed over the last 10 samples. The convergence trend demonstrates a progressive increase in performance as the optimizer explores more effective actuation parameters. The full set of 400 iterations was completed over approximately six hours of experimental time, highlighting the feasibility of real-time optimization within practical time constraints.

3.1 Comparison of Uncontrolled and Optimally Controlled Cases

The uncontrolled and optimally controlled jet configurations are now compared to assess the impact of the control strategy on the flow dynamics. For both cases, extended EBIV acquisitions were carried out and post-processed using a multi-frame PIV algorithm with a seven-image stencil. From each dataset, 10,000 time-resolved velocity snapshots — corresponding to approximately 600 convective time units — were extracted and used to compute and compare key flow characteristics.

The optimal control configuration corresponds to actuation parameters $(f_3, f_6, \Delta\phi) = (63\,\text{Hz}, 31\,\text{Hz}, 207^\circ)$, which translate to non-dimensional Strouhal numbers of $(St_3, St_6) = (0.34, 0.7)$. The point is reported also in the map Fig.3 as the white diamond.

Figure 4 presents a comparison between the uncontrolled and optimally controlled jet configurations. The left panels show the spatial distribution of the ensemble-averaged TKE. The uncontrolled case (top) exhibits a more symmetric and confined distribution, while the optimally controlled case (bottom) displays enhanced energy levels and the development of off-axis high-TKE structures, consistent with the imposed actuation. Note that the color scales differ between the two plots to better resolve each flow's features.

The right panel shows the Power Spectral Density (PSD) of the streamwise velocity fluctuations at the point $(x/D, y/D) = (2.5, 0)$, marked by a white circle in the TKE maps. The optimally controlled case presents a pronounced peak at the actuation frequency and its harmonics. In contrast, the uncontrolled case shows a broader, less energetic spectrum typical of natural jet dynamics.

To further analyze the spatial footprint of the coherent structures observed in the spectral analysis, Spectral Proper Orthogonal Decomposition (SPOD) is applied at three selected frequencies: 30 Hz, 63 Hz, and 96 Hz, corresponding to Strouhal numbers $St \approx 0.33$, 0.7, and 1.06, respectively. These frequencies were chosen based on the prominent peaks identified in the PSD shown in Figure 4 (right). SPOD provides a frequency-resolved modal decomposition of the flow, and the first mode at each frequency represents the most energetic and spatially coherent structure associated with that oscillation (Lumley, 1981; Towne et al., 2018). This makes it particularly suited to highlight how actuation alters the dominant flow organization across different spectral bands. Notably, SPOD has also been shown to be equivalent to resolvent analysis under certain statistical assumptions — specifically, when the expan-

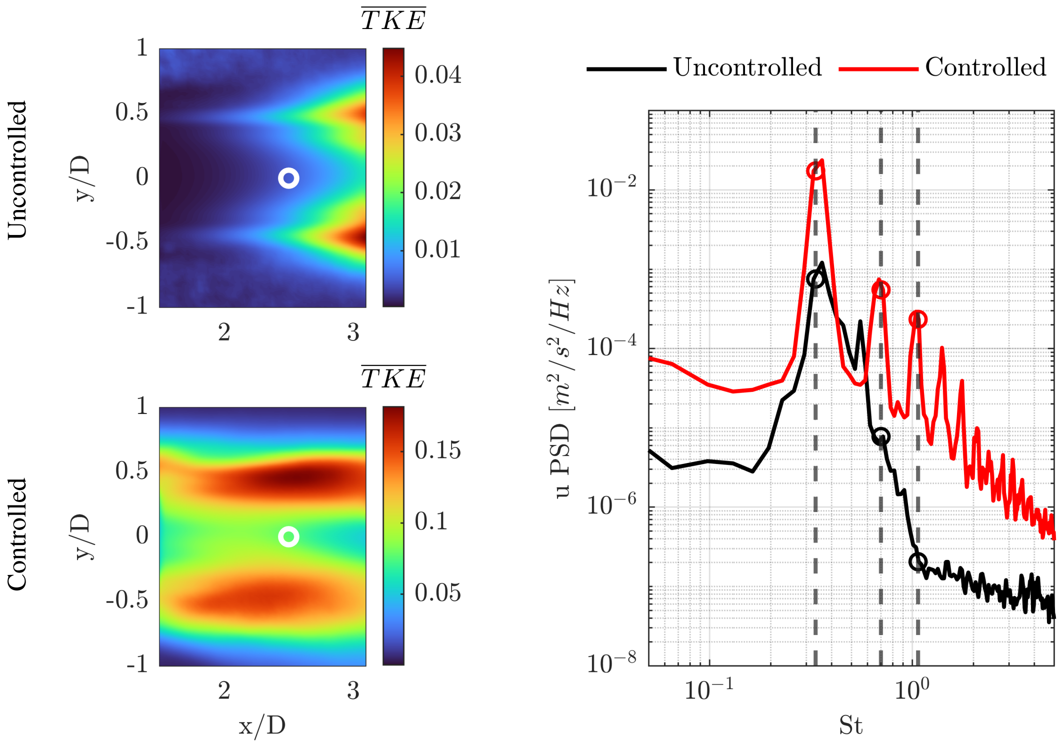

Figure 4: Left: ensemble-averaged turbulent kinetic energy ($\overline{\text{TKE}}$) maps for the uncontrolled (top) and optimally controlled (bottom) jet configurations. The white circle indicates the location $(x/D, y/D) = (2.5, 0)$ used for spectral analysis. Right: PSD of the streamwise velocity fluctuations at the marked location for both cases. Vertical dashed lines indicate selected Strouhal numbers for which SPOD modes are extracted and shown in the following analysis.

sion coefficients are uncorrelated, SPOD and resolvent modes become identical, as discussed by Towne et al. (2018).

Figure 5 displays the leading SPOD mode at the selected frequencies for the uncontrolled (top row) and controlled (bottom row) jets. Each mode is represented through vorticity fields with overlaid velocity vectors. At $St \approx 0.33$, both cases exhibit coherent structures associated with the natural vortex shedding. In the uncontrolled case, the mode shows the classical shear-layer pattern, with extended regions of opposite-signed vorticity stacked vertically across the jet, indicating shear roll-up along both sides of the jet axis. In contrast, the controlled case presents a lower amplitude but more compact and localized structures.

At $St \approx 0.7$, the SPOD mode in the controlled case exhibits compact and well-organized vortical structures primarily located in the shear layers. Additionally, some coherent activity begins to emerge within the inner region of the jet, although it remains relatively weak. This suggests that the actuation at this frequency is not only reinforcing the shear-layer dynamics but also starting to influence the jet core. In contrast, the uncontrolled case shows a low-energy, disordered mode.

At the highest examined frequency, $St \approx 1.06$, the SPOD mode for the uncontrolled jet shows some residual spatial coherence, but the associated energy is low. Noise contamination becomes more evident, particularly in the outer regions of the jet, consistent with the spectral plateau observed in the PSD. In contrast, the controlled case exhibits strong and well-defined vortical structures, not only within the shear layers but also extending into the jet core. The presence of such coherent activity at a frequency that was not directly excited by the actuation suggests the emergence of nonlinear interactions or harmonic responses that amplify energy at higher spectral components. However, further analysis is required to confirm the nature and origin of these mechanisms.

These results confirm that the optimal actuation excites a broader range of organized flow structures, whereas the uncontrolled flow exhibits coherent content only at its natural shedding frequency.

4 Conclusions

This study demonstrates the successful integration of EBIV within a jet flow control experiment, supporting the optimization of open-loop actuation strategies. The EBIV approach enabled time-resolved,

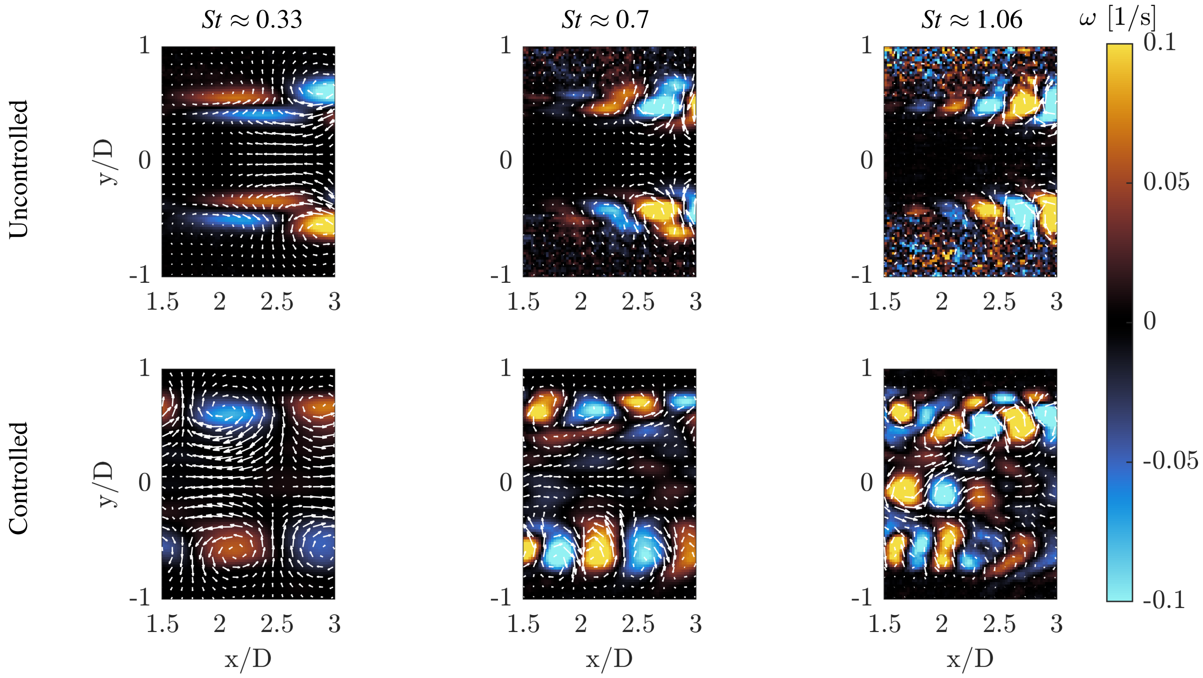

Figure 5: First SPOD mode for the uncontrolled (top) and optimally controlled (bottom) jet at three selected frequencies: 30 Hz ($St \approx 0.33$), 63 Hz ($St \approx 0.7$), and 96 Hz ($St \approx 1.06$). Vorticity fields are shown with overlaid velocity vectors.

full-field velocity measurements at kilohertz rates using a low-power laser module, offering a cost-effective and efficient alternative to traditional high-speed PIV systems.

The reduced data bandwidth and asynchronous acquisition of EBIV allowed for rapid estimation of flow fields and supported the evaluation of control performance through a turbulence-based reward function. Unlike classical approaches relying on point-wise or intrusive sensing, this method leveraged topological information from the entire flow field, enabling a richer understanding of flow structures.

The control optimization revealed that tailored actuation can enhance mixing and promote the emergence of coherent structures across a wider spectral range. The findings underline the potential of EBIV as a compact, high-throughput measurement technique to support efficient flow control strategies.

This work opens the path toward future developments in sensing-assisted flow control using event-based cameras, with promising applications in more complex configurations and closed-loop frameworks.

Acknowledgements

This project has received funding from the European Research Council (ERC) under the European Union’s Horizon 2020 research and innovation programme (grant agreement No 949085, NEXTFLOW ERC StG).

References

Audiffred DB, Cavalieri AV, Maia IA, Martini E, and Jordan P (2024) Reactive experimental control of turbulent jets. *Journal of Fluid Mechanics*

Blanchard AB, Cornejo Maceda GY, Fan D, Li Y, Zhou Y, Noack BR, and Sapsis TP (2021) Bayesian optimization for active flow control. *Acta Mechanica Sinica* pages 1–13

Brunton SL and Noack BR (2015) Closed-loop turbulence control: Progress and challenges. *Applied Mechanics Reviews*

Franceschelli L, Willert CE, Raiola M, and Discetti S (2024) An assessment of event-based imaging velocimetry for online dimensionality reduction in turbulent flows. *arXiv preprint*

Gallego G, Delbrück T, Orchard G, Bartolozzi C, Taba B, Censi A, Leutenegger S, Davison AJ, Conradt J, Daniilidis K, and Scaramuzza D (2022) Event-based vision: A survey. *IEEE Transactions on Pattern Analysis and Machine Intelligence* 44:154–180

Garnett R (2023) *Bayesian Optimization*. Cambridge University Press

Gutmark E and Ho CM (1983) Preferred modes and the spreading rates of jets. *The Physics of fluids* 26:2932–2938

Hussain AF and Zaman K (1981) The 'preferred mode' of the axisymmetric jet. *Journal of fluid mechanics* 110:39–71

Lumley JL (1981) Coherent structures in turbulence. in *Transition and turbulence*. pages 215–242. Elsevier

Mallor F, Semprini-Cesari G, Mukha T, Rezaeiravesh S, and Schlatter P (2024) Bayesian optimization of wall-normal blowing and suction-based flow control of a naca 4412 wing profile. *Flow, Turbulence and Combustion*

Moreno JR, Franceschelli L, De la Prida D, Azpicueta-Ruiz LA, and Raiola M (2024) Implementation of a jet collector and dissipation cavity into a closed anechoic chamber for jet noise studies. in *30th AIAA/CEAS Aeroacoustics Conference (2024)*. page 3066

Parekh D, Kibens V, Glezer A, Wiltse J, and Smith D (1996) Innovative jet flow control-mixing enhancement experiments. in *34th Aerospace Sciences Meeting and Exhibit*. page 308

Shaqarin T, Jiang Z, Wang T, Hou C, Cornejo Maceda GY, Deng N, Gao N, and Noack BR (2024) Jet mixing optimization using a bio-inspired evolution of hardware and control. *Scientific Reports*

Towne A, Schmidt OT, and Colonius T (2018) Spectral proper orthogonal decomposition and its relationship to dynamic mode decomposition and resolvent analysis. *Journal of Fluid Mechanics* 847:821–867

Willert C (2023) Event-based imaging velocimetry using pulsed illumination. *Experiments in Fluids*

Zhou Y, Fan D, Zhang B, Li R, and Noack BR (2020) Artificial intelligence control of a turbulent jet. *Journal of Fluid Mechanics* 897:A27